

PAPER

Solution-processed photodetectors based on organic–inorganic hybrid perovskite and nanocrystalline graphite

To cite this article: Yan Wang *et al* 2016 *Nanotechnology* **27** 175201

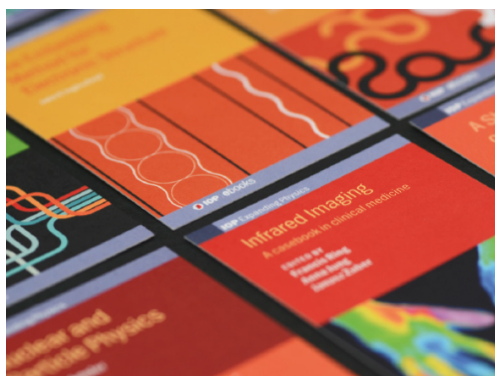
View the [article online](#) for updates and enhancements.

Related content

- [High performance photodetector based on 2D \$\text{CH}_3\text{NH}_3\text{PbI}_3\$ perovskite nanosheets](#)
Pengfei Li, B N Shivananju, Yupeng Zhang *et al*.
- [Enhanced optoelectronic quality of perovskite films with excess \$\text{CH}_3\text{NH}_3\text{I}\$ for high-efficiency solar cells in ambient air](#)
Yunhai Zhang, Huiru Lv, Can Cui *et al*.
- [Enhanced performance of solution-processed broadband photodiodes by epitaxially blending \$\text{MAPbBr}_3\$ quantum dots and ternary \$\text{PbS}_x\text{Se}_{1-x}\$ quantum dots as the active layer](#)
Muhammad Sulaman, Shengyi Yang, Yurong Jiang *et al*.

Recent citations

- [Self-powered broadband photodetector based on a solution-processed p-NiO/n-CdS:Al heterojunction](#)
Chandra Sekhar Reddy K *et al*
- [Photostimulated Near-Resonant Charge Transport over 60 nm in Carbon-Based Molecular Junctions](#)
Shailendra K. Saxena *et al*
- [The dependence of optoelectric performance on channel length in photodetectors with MBE CdTe single-crystalline thin films on perovskite \$\text{SrTiO}_3\$](#)
Zhiqiang Pan *et al*



IOP | ebooks™

Bringing together innovative digital publishing with leading authors from the global scientific community.

Start exploring the collection—download the first chapter of every title for free.

Solution-processed photodetectors based on organic–inorganic hybrid perovskite and nanocrystalline graphite

Yan Wang¹, Zhonggao Xia¹, Songnan Du¹, Fang Yuan¹, Zigang Li¹,
Zhenjun Li², Qing Dai², Haolan Wang³, Shiqiang Luo⁴,
Shengdong Zhang¹ and Hang Zhou¹

¹ Shenzhen Key Lab of Thin Film Transistor and Advanced Display, Peking University Shenzhen Graduate School, Peking University, Shenzhen, People's Republic of China

² National Center for Nanoscience & Technology, Beijing, People's Republic of China

³ Shenzhen Bronze Technologies Ltd, Shenzhen, People's Republic of China

⁴ School of Energy and Environment, City University of Hong Kong, Hong Kong, People's Republic of China

E-mail: zhouh81@pkusz.edu.cn

Received 23 November 2015, revised 10 February 2016


Accepted for publication 22 February 2016

Published 15 March 2016



Abstract

We present here solution-processed photodetectors based on a methyl ammonium lead iodide perovskite (MAPbI₃) and nanocrystalline graphite (NCG) hybrid composite. The highest responsivity of the best MAPbI₃/NCG photodetector was 795 mA W⁻¹ at 500 nm visible light, which is almost twice as high as that of the NCG-free MAPbI₃ photodetector (408 mA W⁻¹). The enhanced performance of the MAPbI₃/NCG photodetector arises from the improved charge extraction at the MAPbI₃/NCG interface. The dependence of photodetector performance on the mass percentage of NCG (the ratio of NCG to MAPbI₃) in the hybrid materials is also reported here, and is correlated to the fabrication process. Moreover, by comparing the responsivity of the devices with different channel lengths, we show that the performance of hybrid photodetectors can be further tuned by tailoring the channel length.

 Online supplementary data available from stacks.iop.org/NANO/27/175201/mmedia

Keywords: nanocrystalline graphite, activation energy, perovskite photodetectors, organic–inorganic hybrid

(Some figures may appear in colour only in the online journal)

1. Introduction

Organolead halide perovskite solar cells have shown substantial improvement in their power conversion efficiency in recent years [1–6]. The rapid development of high-efficiency perovskite solar cells has, at the same time, aroused research enthusiasm for high-performance perovskite-based photodetectors [7–11]. One attractive property of organolead halide perovskites is that they can be deposited via low-cost solution-processing techniques such as drop-casting, spray-coating, spin-coating and doctor-blading [12–15]. In addition, the band gap of the solution-processed perovskite can be

effectively tuned by arranging different halide anions and the organic amide constituent, allowing specific photodetection designed for selected wavelength ranges [16–18]. Moreover, the constituent lead ions, having a large atomic number, further enable its application in x-ray detection [19]. All these advanced properties of organolead halide perovskite render the materials with vast application potential, ranging from medical x-ray imaging to visible light communication.

An organic–inorganic hybrid approach is frequently reported in organic photodetectors for performance enhancement [7]. Similar approaches have also been applied to perovskite photodetectors, where the responsivity as well as the

rise and delay time of the detector are improved by chemical decoration with graphene oxide (from 11.1 mA W⁻¹, 53.5 ms, 69.6 ms to 73.9 mA W⁻¹, 40.9 ms, 28.8 ms, respectively) [9]. It has been confirmed that hybrid photoconductors have benefited from efficient charge carrier separation and transport on the inorganic–organic interface [20, 21]. However, the dependence of hybrid device performance on the amount of graphene oxide addition remains unclear. Furthermore, the responsivity is not as high as other reported values [22, 23]. An alternative detector structure is based on perovskite–graphene stacking structures, although it reaches a responsivity of 2×10^6 A W⁻¹, and shows an unexpectedly slow transient response (55 and 75 s) [21]. The performance parameters of reported planar structure perovskite photodetectors are listed in the supplementary material (table S1).

Here, we introduce for the first time nanocrystalline graphite (NCG) particles into a perovskite composite to study its effect on the performance of solution-processed perovskite photodetectors. We demonstrate that the solution-processed photodetectors based on perovskite and NCG can achieve relatively high performance (795 mA W⁻¹, 25 and 25 ms) and we elucidate the photoconductive performance dependence on the NCG-content. To our knowledge, this is one of the highest values for photoconductor-type perovskite photodetector, while maintaining a fast transient response time. Furthermore, we show that the responsivity of the NCG-perovskite composite photodetectors is improved by adjusting the channel length of the photoconductor-type detectors.

2. Experimental section

2.1. Materials

The perovskite precursor was synthesized with a procedure reported previously [24]. CH₃NH₃I was synthesized by mixing 24 ml of methylamine (33% in methanol, Aladdin) with 10 ml of hydroiodic acid (57% in water, Aladdin) in a round-bottom flask at 0 °C for 2 h with stirring. The solvent was removed by heating the solution in a rotary evaporator at 50 °C. The white precipitate of raw CH₃NH₃I was washed with ethanol, filtered and then washed with diethyl ether. This procedure was repeated three times. After the last filtration, the products were dried at 60 °C in a vacuum oven for 24 h. A 40 wt. % solution of CH₃NH₃PbI₃ was prepared by mixing PbI₂ (99%, Sigma) and CH₃NH₃I in a 1:1 molar ratio in N, N-dimethylformamide (DMF, Sigma) and heating at 70 °C overnight inside a nitrogen-filled glove box. Nanocrystalline graphite was produced by the arc discharge method under an Ar atmosphere. In this method, an arc was triggered in-between a 6 mm diameter carbon rod, which served as the anode, and a 20 mm diameter carbon rod as the cathode. The discharge current and voltage were 300 A at 40 V, respectively. During this process, 760 Torr Ar was introduced into the reaction chamber as the quenching media. The process was automatically controlled by feeding the anodic carbon rod to keep a sustainable arc, and the consumption rate of the carbon rod was approximately 8 g min⁻¹. The perovskite precursors

with nanocrystalline graphite were prepared by adding different mass percentages of nanocrystalline graphite into the perovskite precursors, then the solutions were ultrasonicated for 1 h to allow thorough dispersion of the nanocrystalline graphite. Polymethylmethacrylate (PMMA) (average molecular weight ~120 000 g mol⁻¹ by gel permeation chromatography, Aldrich), which was used as the encapsulation layer, was dissolved in n-Butyl acetate (Aladdin) at a concentration of 8 wt. % and stirred at 60 °C overnight.

2.2. Device fabrication

The glass substrates were sequentially cleaned in soap water, deionized water, acetone, and ethanol in an ultrasonic bath for 10 min, and dried under nitrogen flow. The electrode (Cr/Au, 8 nm/80 nm) was then thermally evaporated on the glass substrates through a shadow mask, defining the channel length which ranged from 40 to 100 μm, and the ratio of width to length of all the patterns was 10. The substrates were treated with O₂ plasma for 10 min (75 W) before transferring them to the glove box for deposition of the perovskite layer. The perovskite precursor was spin-coated at 3000 rpm for 40 s on the substrate. After a few seconds delay, two drops of toluene were quickly added during the spin-coating procedure to improve the film morphology. The substrates were then heated on a hot plate at 100 °C for 20 min. To improve the device stability in air, layers of PMMA were spin-coated onto the perovskite films at 4000 rpm for 60 s. Finally, the devices were heated on a hot plate at 80 °C for 10 min.

2.3. Device characterization

X-ray diffraction (XRD) pattern data were collected with a Bruker D8 Advance diffractometer with nickel-filtered Cu Kα radiation ($\lambda = 1.5406$ Å) operating at 40 kV and 40 mA. Raman spectra were obtained on a Renishaw inVia Raman spectrometer using a He-Cd laser (514 nm). Optical absorption of the film was tested by UV–vis absorption spectra (UV-2600, Shimadzu). The contact angle (CA) was measured by a Theta Lite Optical Tensiometer TL 100. Scanning electron microscopy (SEM) images were acquired on a TESCAN field-emission SEM. Photoluminescence (PL) spectra were obtained using a 1 K series He-Cd laser. The performance of the photodetectors was evaluated using an Agilent B1500 semiconductor analyzer with 500 nm monochromatic light from a 500 W Xe lamp.

3. Results and discussion

We first characterized our NCG nanoparticles by transmission electron microscopy (TEM) and Raman measurements. The TEM images given in the supplementary material (figure S1) indicates that the NCG particles are several tens of nanometers in diameter, whereas the Raman spectra (figure S2) present bands at 1346 and 1575 cm⁻¹, corresponding to the D and G bands of graphite, respectively.

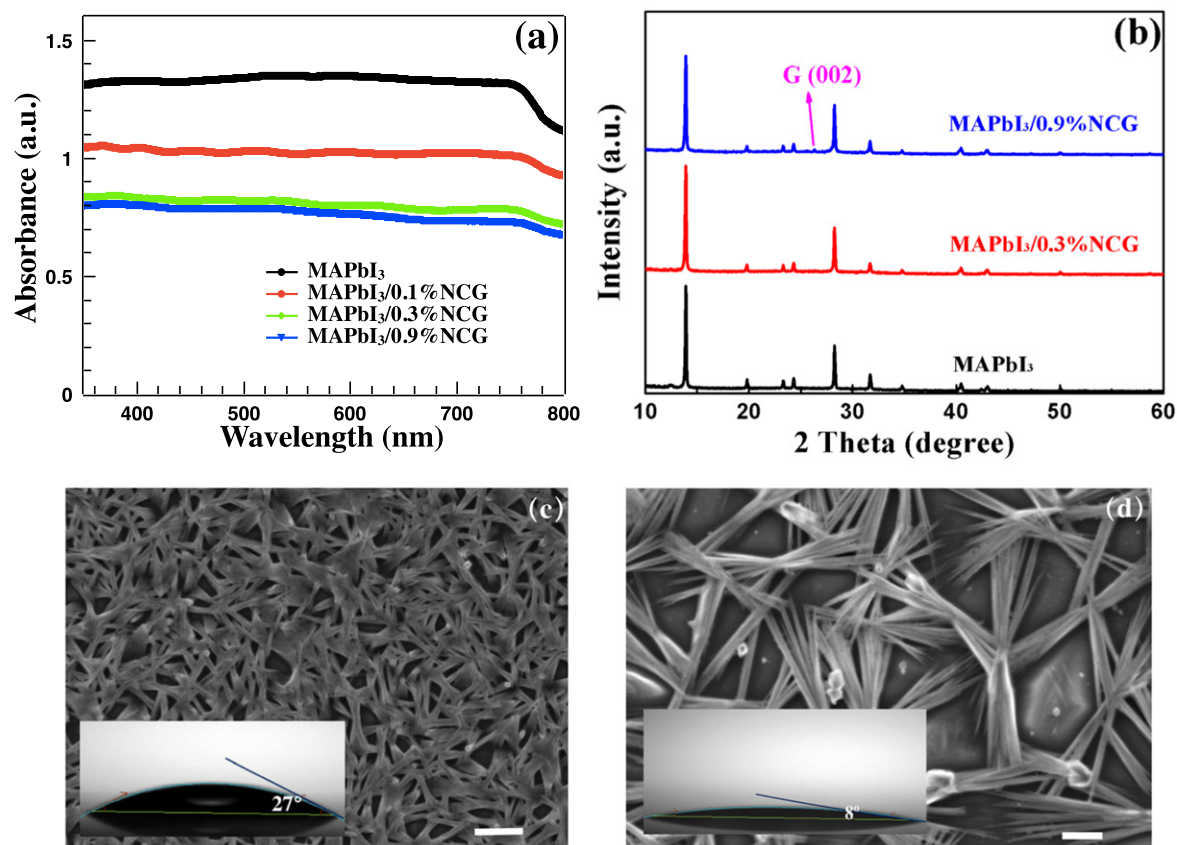


Figure 1. (a) Absorbance of the perovskite and the hybrid layers. (b) XRD patterns of the layers. (c) SEM of pure perovskite layer. (d) SEM of perovskite with 0.9 wt. % NCG layer. Insets are CAs of the precursors on glass, the scale bar is 50 μm .

Figure 1(a) shows the absorbance of the four different mass percentages for the NCG constituent perovskite thin-film samples deposited by the same spin-coating method. The resultant absorbance of the hybrid thin films was lower than that of the pure perovskite thin-film sample. The difference became more significant when the mass percentage of NCG was higher than 0.3%. One possible reason that led to the change of MAPbI₃/NCG absorbance could be that the thin-film thickness is changed somehow under the same fabrication technique. Indeed, we observed the change of the thin-film average thickness using a profilometer. We suspect that the NCG additive could have changed the hydrophobicity of the perovskite precursor. In order to verify our assumption, we investigated the precursor's hydrophobicity by comparing the CAs of all the different precursors on glass substrates. Details of the CA measurement results are given in the supplementary material (figure S3). Briefly, we confirmed that the CA decreased as the mass percentage of NCG increased. The inset of figures 1(c)–(d) show the CA of the droplets from the precursor with and without NCG. The CA of the precursor with 0.9 wt. % NCG is $\sim 8^\circ$, much less than the CA of the neat perovskite precursor ($\sim 27^\circ$). The precursor with NCG became more hydrophilic, which led to thinner films under the same spin-coating conditions. We also examined the XRD of the perovskite layers with different mass percentages of NCG. As shown in figure 1(b), the layers all showed strong peaks at 14.05° , 19.94° , 23.44° , 24.44° , 28.38° , 30.89° ,

31.82° , 40.42° and 43.03° , corresponding to the reflections from (110), (112), (211), (202), (220), (213), (310), (224) and (314) lattice planes of the tetragonal perovskite structure with $a = 8.874 \text{ \AA}$ and $c = 12.671 \text{ \AA}$. The intensity of the XRD peaks of MAPbI₃ and MAPbI₃/NCG remained almost the same, indicating no structural change in the crystallinity of the hybrid material. In particular, for the sample with 0.9 wt. % NCG, there was a small peak at about 26.3° , which indicated the presence of NCG in the film [25]. This peak became insignificant in the smaller mass percentage of NCG composite films. Figures 1(c)–(d) also present the surface morphologies of our spin-coated perovskite thin films under SEM, which helped us evaluate the influence of NCG addition on the morphology of the perovskite film. The pure perovskite film shown in figure 1(c) had a long fibril-like structure, similar to a disoriented mat with overlapping fibrils, which is consistent with the structure reported by other groups employing the same deposition method [26, 27]. The fibril of the hybrid film shown in figure 1(d) became much larger with 0.9 wt. % of NCG additives. Larger fibrils were observed for larger NCG mass percentages in the precursor. Moreover, some large electron-scattering domains became significant when the mass percentage of NCG was over 0.9%, which could be due to the presence of the NCG agglomeration. The SEM images of films with increasing amounts of NCG are also given in the supplementary material (figure S4).

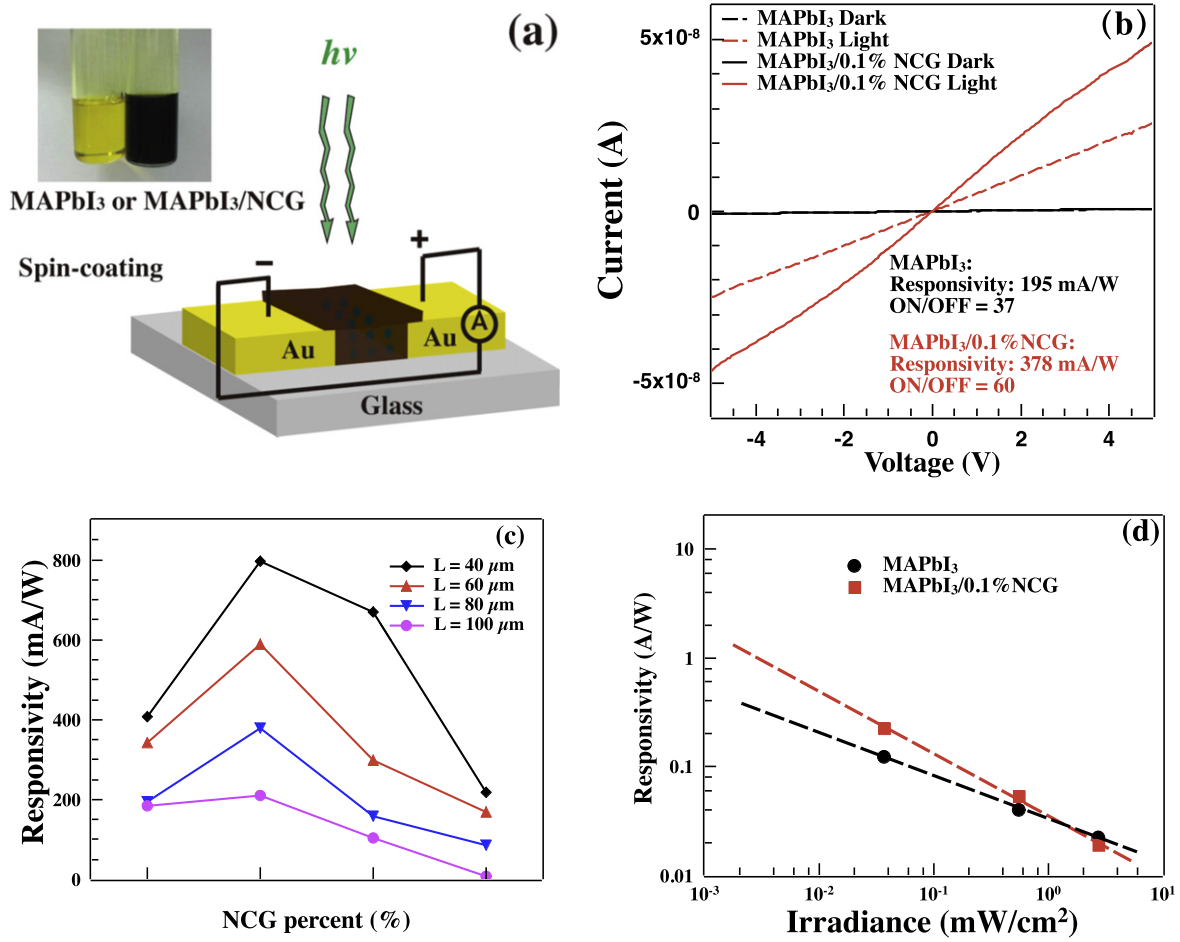


Figure 2. (a) Structure of the photodetector device. The inset is the photograph of the MAPbI₃ and MAPbI₃/NCG precursors. (b) *I*-*V* curves of MAPbI₃ and MAPbI₃/NCG (0.1 wt. %) in the dark and under light illumination at 500 nm with an intensity of 0.2 mW cm⁻². The inset is the responsivity and ON/OFF ratio results at 5 V. (c) Responsivity of the MAPbI₃ and MAPbI₃/NCG hybrid photodetectors with channel lengths ranging from 40 to 100 μm. (d) Responsivity as a function of the irradiance for the MAPbI₃ and MAPbI₃/NCG (0.1% wt) hybrid photodetectors with a 60 μm channel length.

As shown in figure 2(a), the photoconductor-type photodetectors comprise perovskite or perovskite/NCG layers deposited from the solution process. The photo-responsivity of these detectors was evaluated under light illumination at 500 nm with an intensity of 0.2 mW cm⁻². Plots of typical linear and symmetrical photocurrent versus voltage shown in figure 2(b) indicate that the MAPbI₃ and MAPbI₃/NCG hybrids form ohmic contacts with the Au electrodes. For devices with a channel length of 80 μm biased at 5 V, the dark currents of the MAPbI₃ device and MAPbI₃/NCG hybrid device are almost equivalent to each other, which are 0.7 nA for the MAPbI₃ device, and 0.8 nA for the MAPbI₃/NCG (0.1 wt. %) device, respectively. With higher constitution of NCG in MAPbI₃, the dark current increases to over 1 nA due to the increasing amount of conductive NCG. Under illumination, the MAPbI₃/NCG (0.1 wt. %) photodetector gives much better performance than the MAPbI₃ device in terms of both responsivity and ON/OFF ratio.

We then further investigated the photodetectors' performance with different photoconductor channel lengths. As the

gain (*G*) of the photodetector is determined by:

$$G = \frac{\tau}{L^2/\mu V}$$

where *L* is the channel length, *V* is the applied bias, *μ* is the carrier mobility and *τ* is the lifetime. The responsivity can be calculated from the gain by:

$$R = \frac{G}{E_{hv}}$$

where *E_{hv}* is the energy of incident photo. To a certain device, its gain or responsivity is most sensitive to the channel length, increasing rapidly with decreasing channel length. The responsivity of the MAPbI₃ and MAPbI₃/NCG hybrid photodetectors with channel lengths ranging from 40 to 100 μm are presented in figure 2(c). As predicted by the above equation, devices with a shorter channel length gave higher photoresponse for a certain perovskite composite. It can also be found in figure 2(c) that devices with different channel lengths show similar NCG-dependent responsivity, demonstrating significant enhancement at low addition of NCG. The responsivity reached 795 mA W⁻¹ for the device

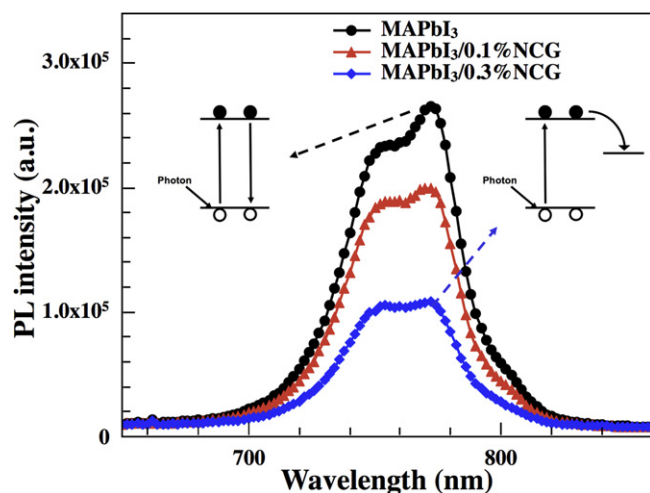


Figure 3. Comparison of PL spectra of the neat $\text{CH}_3\text{NH}_3\text{PbI}_3$ and $\text{CH}_3\text{NH}_3\text{PbI}_3/\text{NCG}$ hybrids.

with 0.1 wt. % NCG and with a $40\ \mu\text{m}$ channel length, which is twice as high as that of its NCG-free counterpart. We suspect that the enhanced performance of the low-percentage NCG photodetector is related to the improved photo-induced free carrier transport, particularly for electrons. The electron mobility could have been increased by the tiny amount of metallic NCG in the film, and the photo-conductivity increased accordingly. However, for the device with a channel length of $100\ \mu\text{m}$, the enhancement becomes insignificant even for the 0.1 wt. % NCG device. The device performance, in this case, could have been limited by its hole conduction. It is worth emphasizing that the hybrid film is actually thinner than the pure perovskite device. The thinner hybrid film obviates the possibility of absorption of more light. We noted that excessive NCG decreases the absorbance of the hybrid film, thus reducing the overall photocurrent. In other words, the responsivity decreased with thinner thickness, which is in accordance with the evidence given in the research of Deng *et al* [23]. Therefore, for NCG mass percentage above 0.9%, the responsivity of all the devices at a certain channel length was lower than that of their pure perovskite counterparts.

Photosensitivity dependence of the MAPbI_3 and $\text{MAPbI}_3/\text{NCG}$ hybrids on light intensity has also been explored. The current-voltage curves of the device were measured under illumination with 500 nm light at different power intensities from 0.0037 to $2.75\ \text{mW cm}^{-2}$ for a fixed channel length of $60\ \mu\text{m}$. Biased at 5 V, the photo current increased gradually with the increase in light intensity. The compared results of the relationship between responsivity and incident irradiance are shown in figure 2(d). Both the MAPbI_3 and $\text{MAPbI}_3/\text{NCG}$ hybrid photodetectors had the tendency to increase responsivity with a decrease in irradiance. It is concluded that $\text{MAPbI}_3/\text{NCG}$ hybrid photodetectors are more sensitive to weak light, and higher responsivity can be achieved under weak light illumination, which is consistent with the results found for the reported photovoltaic-type perovskite detectors [8, 28].

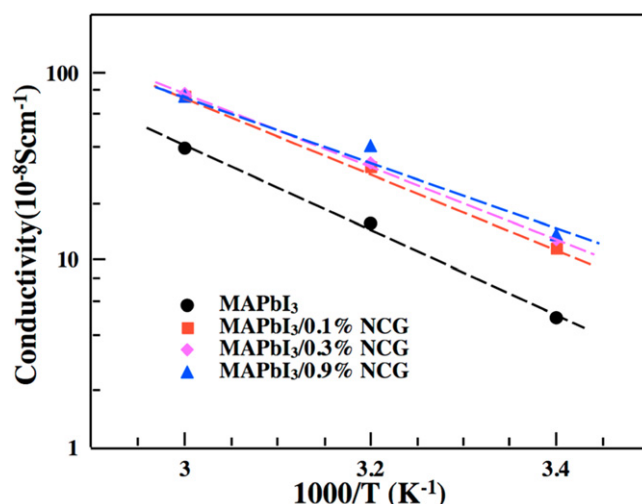


Figure 4. The conductivity of the MAPbI_3 and $\text{MAPbI}_3/\text{NCG}$ films as a function of temperature.

Steady-state PL emission spectra were adopted to further elucidate the role of NCG in the $\text{MAPbI}_3/\text{NCG}$ hybrid. As shown in figure 3, the dominant peak located at 772 nm corresponds to the optical band gap of the MAPbI_3 perovskite films ($\sim 1.6\ \text{eV}$), which can be attributed to the band-to-band recombination [29]. Another peak at 750 nm comes from our glass substrate whose PL spectra are shown in the supplementary material (figure S5). The PL intensity of the $\text{MAPbI}_3/\text{NCG}$ hybrid decreased with increasing the NCG addition amount in the MAPbI_3 precursor. In the absence of NCG, the photo-induced electron-hole pairs recombination rate in the perovskite was reported to be a few picoseconds [30]; however, with the mediation of NCG, the photo-generated electrons transfer from MAPbI_3 to NCG, decreasing the photo-induced electron-hole band-to-band recombination.

In order to reveal the carrier conduction mechanics of our perovskite thin films, we extracted the activation energies in the MAPbI_3 and $\text{MAPbI}_3/\text{NCG}$ hybrids by studying the influence of NCG on the electrical property of MAPbI_3 and the photodetector performance. The temperature-dependent conductivity of the MAPbI_3 and $\text{MAPbI}_3/\text{NCG}$ hybrids were characterized in the dark with varying substrate temperature. Hybrid halide perovskites are mixed ionic-electronic conductors, and the investigation of their charge transport in the material can provide in-depth understanding of the high photovoltaic performance [31, 32]. The MAPbI_3 and $\text{MAPbI}_3/\text{NCG}$ hybrids all exhibited ohmic-like behavior with almost linear I - V dependence. The conductivity of MAPbI_3 as a function of temperature is presented in figure 4. The data were obtained by biasing the device with 5 V, and were fitted by applying the Arrhenius law:

$$\sigma = A \exp\left(-\frac{E_A}{kT}\right)$$

where A is a constant, E_A is the activation energy, k is the Boltzmann's constant and T the temperature. The Arrhenius equation can be re-written in a logarithm form to extract the

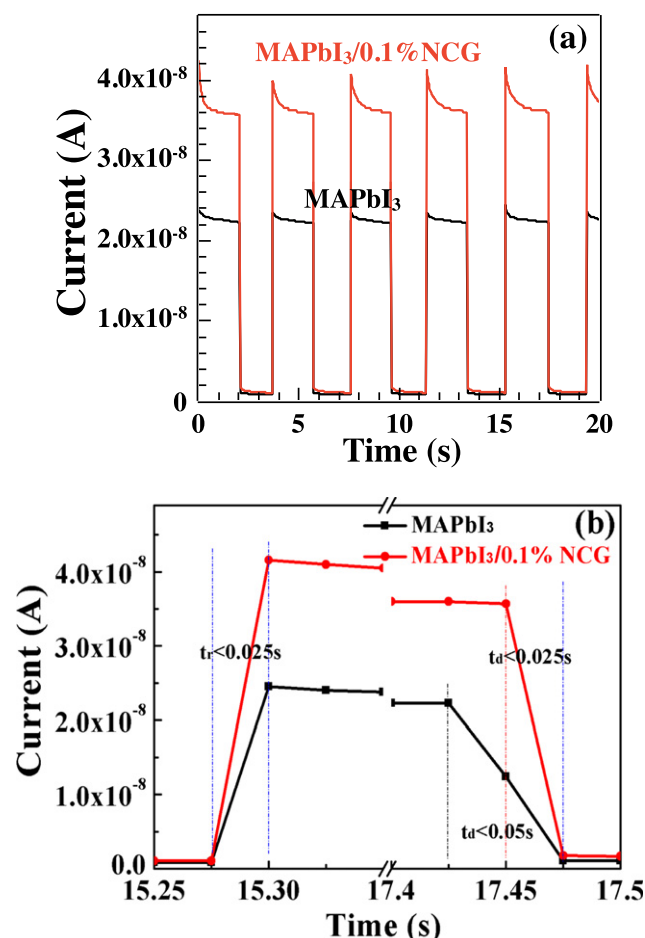


Figure 5. (a) ON-OFF photoresponse of the CH₃NH₃PbI₃ and CH₃NH₃PbI₃/NCG (0.1 wt. %) photodetectors at a bias voltage of 5 V on the time scale of 0–20 s. (b) Photocurrent rise and delay time of the devices.

activation energy:

$$\ln \sigma = \ln A - \frac{E_A}{kT}$$

which represents a straight line whose slope is $-E_A/k$. This offers a simple way of determining the activation energy from values of σ measured at different temperatures [33, 34]. The bulk conductivity of MAPbI₃ increased with temperature with an activation of 0.44 eV, in agreement with previous research reported [31, 35]. Calculated activation energies for ionic migration in MAPbI₃ are 0.58, 2.13 and 0.84 eV for I⁻, Pb²⁺ and CH₃NH₃⁺, respectively [32]. The much lower activation energy of 0.44 eV deduced from our results indicates electronic drift-diffusion migration as the main transport mechanism.

The conductivity of the MAPbI₃/NCG hybrid was higher than the conductivity of MAPbI₃ due to the constitution of metallic NCG. As can be seen from figure 4, the conductivity of both MAPbI₃/NCG and MAPbI₃ increase with increasing temperature, showing a typical semiconductor characteristic. The MAPbI₃/NCG hybrid exhibited a gentler slope with increasing the component of NCG. The activation energy decreased with increasing NCG in the perovskite, with 0.4,

0.386, and 0.368 eV extracted values from the sample with the NCG mass percentage of 0.1, 0.3, and 0.9, respectively.

Finally, the transient photoresponse of the MAPbI₃ and MAPbI₃/NCG hybrid photodetectors were under periodic illumination with an ON/OFF interval of 4 s. We present the results of the MAPbI₃ and MAPbI₃/NCG (0.1 wt. %) hybrid photodetectors with a channel length of 80 μ m in figure 5. The results revealed that the photocurrent of both MAPbI₃ and MAPbI₃/NCG were all consistent and repeatable with fast responses. The rise and decay time are defined as when the photocurrent and the dark current increase or decrease by 90% compared to their peak value, respectively. The time response of both photodetectors all showed a rise time of less than 25 ms, which is much faster than previously reported perovskite hybrid photodetectors [36–38]. Moreover, the decay time of MAPbI₃ (less than 50 ms) was a little longer than the MAPbI₃/NCG hybrid (less than 25 ms). The NCG facilitates the free carrier transport, which to some extent accelerates the extraction of electrons and holes trapped in MAPbI₃.

4. Conclusion

We have demonstrated that MAPbI₃/NCG hybrid photodetectors fabricated by spin-coating have higher responsivity, higher ON/OFF and shorter delay time than the neat MAPbI₃ photodetector. The dramatic PL quenching process, lower activation energy and higher conductivity with increasing the amount of NCG in the precursor all indicate efficient charge transfer between MAPbI₃ and NCG. Moreover, shortening the channel length of the devices is an effective approach to achieving higher performance photodetectors. The results not only provide in-depth insight into the electrical property of the structure, but shed light on the future exploration of advanced perovskite–nanocarbon materials and devices.

Acknowledgments

This work was supported by the National Science Fund of China (No.61204077, No.21372023) and the Shenzhen Science and Technology Innovation Fund (JCYJ20150629144006876, No.KQCX20140522143114399).

References

- [1] Wong A B, Lai M, Eaton S W, Yu Y, Lin E, Dou L, Fu A and Yang P 2015 Growth and anion exchange conversion of CH₃NH₃PbX₃ nanorod arrays for light-emitting diodes *Nano Lett.* **15** 5519–24
- [2] Li W, Dong H, Dong G and Wang L 2015 Hysteresis mechanism in perovskite photovoltaic devices and its potential application for multi-bit memory devices *Org. Electron.* **26** 208–12
- [3] Jaramillo-Quintero O A, Sanchez R S, Rincon M and Mora-Sero I 2015 Bright visible-infrared light emitting diodes based on hybrid halide perovskite with spiro-OMeTAD as a hole-injecting layer *J. Phys. Chem. Lett.* **6** 1883–90

- [4] Li G, Tan Z-K, Di D, Lai M L, Jiang L, Lim J H-W, Friend R H and Greenham N C 2015 Efficient light-emitting diodes based on nanocrystalline perovskite in a dielectric polymer matrix *Nano Lett.* **15** 2640–4
- [5] Xu X, Li S, Zhang H, Shen Y, Zakeeruddin S M, Graetzel M, Cheng Y-B and Wang M 2015 A power pack based on organometallic perovskite solar cell and supercapacitor *ACS Nano* **9** 1782–7
- [6] Xing J, Liu X F, Zhang Q, Ha S T, Yuan Y W, Shen C, Sum T C and Xiong Q 2015 Vapor phase synthesis of organometal halide perovskite nanowires for tunable room-temperature nanolasers *Nano Lett.* **15** 4571–7
- [7] Wang X, Song W, Liu B, Chen G, Chen D, Zhou C and Shen G 2013 High-performance organic-inorganic hybrid photodetectors based on P3HT: CdSe nanowire heterojunctions on rigid and flexible substrates *Adv. Funct. Mater.* **23** 1202–9
- [8] Liu C, Wang K, Du P, Wang E, Gong X and Heeger A J 2015 Ultrasensitive solution-processed broad-band photodetectors using $\text{CH}_3\text{NH}_3\text{PbI}_3$ perovskite hybrids and PbS quantum dots as the light harvesters *Nanoscale* **7** 16460–9
- [9] He M, Chen Y, Liu H, Wang J, Fang X and Liang Z 2015 Chemical decoration of $\text{CH}_3\text{NH}_3\text{PbI}_3$ perovskites with graphene oxides for photodetector applications *Chem. Commun.* **51** 9659–61
- [10] Voznyy O, Zhitomirsky D, Stadler P, Ning Z, Hoogland S and Sargent E H 2012 A charge-orbital balance picture of doping in colloidal quantum dot solids *ACS Nano* **6** 8448–55
- [11] Sukhovatkin V, Hinds S, Brzozowski L and Sargent E H 2009 Colloidal quantum-dot photodetectors exploiting multiexciton generation *Science* **324** 1542–4
- [12] Xing G, Mathews N, Sun S, Lim S S, Lam Y M, Grätzel M, Mhaisalkar S and Sum T C 2013 Long-range balanced electron- and hole-transport lengths in organic-inorganic $\text{CH}_3\text{NH}_3\text{PbI}_3$ *Science* **342** 344–7
- [13] Wehrenfennig C, Eperon G E, Johnston M B, Snaith H J and Herz L M 2014 High charge carrier mobilities and lifetimes in organolead trihalide perovskites *Adv. Mater.* **26** 1584–9
- [14] Stranks S D, Eperon G E, Grancini G, Menelaou C, Alcocer M J P, Leijtens T, Herz L M, Petrozza A and Snaith H J 2013 Electron-hole diffusion lengths exceeding 1 micrometer in an organometal trihalide perovskite absorber *Science* **342** 341–4
- [15] Shi D *et al* 2015 Low trap-state density and long carrier diffusion in organolead trihalide perovskite single crystals *Science* **347** 519–22
- [16] Eperon G E, Stranks S D, Menelaou C, Johnston M B, Herz L M and Snaith H J 2014 Formamidinium lead trihalide: a broadly tunable perovskite for efficient planar heterojunction solar cells *Energy Environ. Sci.* **7** 982–8
- [17] Xing G, Mathews N, Lim S S, Yantara N, Liu X, Sabba D, Grätzel M, Mhaisalkar S and Sum T C 2014 Low-temperature solution-processed wavelength-tunable perovskites for lasing *Nat. Mater.* **13** 476–80
- [18] Chen Z, Li H, Tang Y, Huang X, Ho D and Lee C-S 2014 Shape-controlled synthesis of organolead halide perovskite nanocrystals and their tunable optical absorption *Mater. Res. Express* **1** 015034
- [19] Yakunin S *et al* 2015 Detection of x-ray photons by solution-processed lead halide perovskites *Nat. Photonics* **9** 444–9
- [20] Wang Y *et al* 2015 Hybrid graphene–perovskite phototransistors with ultrahigh responsivity and gain *Adv. Opt. Mater.* **3** 1389–96
- [21] Spina M, Lehmann M, Náfrádi B, Bernard L, Bonvin E, Gaál R, Magrez A, Forró L and Horváth E 2015 Microengineered $\text{CH}_3\text{NH}_3\text{PbI}_3$ nanowire/graphene phototransistor for low-intensity light detection at room temperature *Small* **11** 4824–8
- [22] Hu X, Zhang X, Liang L, Bao J, Li S, Yang W and Xie Y 2014 High-performance flexible broadband photodetector based on organolead halide perovskite *Adv. Funct. Mater.* **24** 7373–80
- [23] Deng H, Yang X, Dong D, Li B, Yang D, Yuan S, Qiao K, Cheng Y-B, Tang J and Song H 2015 Flexible and semitransparent organolead triiodide perovskite network photodetector arrays with high stability *Nano Lett.* **15** 7963–9
- [24] Ball J M, Lee M M, Hey A and Snaith H J 2013 Low-temperature processed meso-superstructured to thin-film perovskite solar cells *Energy Environ. Sci.* **6** 1739–43
- [25] Pang H, Wang X, Zhang G, Chen H, Lv G and Yang S 2010 Characterization of diamond-like carbon films by SEM, XRD and Raman spectroscopy *Appl. Surf. Sci.* **256** 6403–7
- [26] Jeon Y-J, Lee S, Kang R, Kim J-E, Yeo J-S, Lee S-H, Kim S-S, Yun J-M and Kim D-Y 2014 Planar heterojunction perovskite solar cells with superior reproducibility *Sci. Rep.* **4** 6953
- [27] Bastiani M D, D’Innocenzo V, Stranks S D, Snaith H J and Petrozza A 2014 Role of the crystallization substrate on the photoluminescence properties of organo-lead mixed halides perovskites *APL Mater.* **2** 081509
- [28] Dou L, Yang Y (Micheal), You J, Hong Z, Chang W-H, Li G and Yang Y 2014 Solution-processed hybrid perovskite photodetectors with high detectivity *Nat. Commun.* **5** 5404
- [29] Deschler F *et al* 2014 High photoluminescence efficiency and optically pumped lasing in solution-processed mixed halide perovskite semiconductors *J. Phys. Chem. Lett.* **5** 1421–6
- [30] Marchioro A, Teuscher J, Friedrich D, Kunst M, van de Krol R, Moehl T, Grätzel M and Moser J-E 2014 Unravelling the mechanism of photoinduced charge transfer processes in lead iodide perovskite solar cells *Nat. Photonics* **8** 250–5
- [31] Yang T-Y, Gregori G, Pellet N, Grätzel M and Maier J 2015 The significance of ion conduction in a hybrid organic-inorganic lead-iodide-based perovskite photosensitizer *Angew. Chem. Int. Ed Engl.* **54** 7905–10
- [32] Eames C, Frost J M, Barnes P R F, O’Regan B C, Walsh A and Islam M S 2015 Ionic transport in hybrid lead iodide perovskite solar cells *Nat. Commun.* **6** 7497
- [33] Logan S R 1982 The origin and status of the Arrhenius equation *J. Chem. Educ.* **59** 279
- [34] Chiarella F, Ferro P, Licci F, Barra M, Biasiucci M, Cassinese A and Vaglio R 2006 Preparation and transport properties of hybrid organic–inorganic $\text{CH}_3\text{NH}_3\text{SnBr}_3$ films *Appl. Phys. A* **86** 89–93
- [35] Knop O, Wasylischen R E, White M A and Cameron T S 1990 Alkylammonium lead halides: 2. $\text{CH}_3\text{NH}_3\text{PbX}_3$ ($\text{X} = \text{Cl}, \text{Br}, \text{I}$) perovskites: cuboctahedral halide cages with isotropic cation reorientation *Can. J. Chem.* **68** 412–22
- [36] Lee Y, Kwon J, Hwang E, Ra C-H, Yoo W J, Ahn J-H, Park J H and Cho J H 2015 High-performance perovskite–graphene hybrid photodetector *Adv. Mater.* **27** 41–6
- [37] Wang Y *et al* 2015 Hybrid graphene–perovskite phototransistors with ultrahigh responsivity and gain *Adv. Opt. Mater.* **10** 1389–96
- [38] Spina M, Lehmann M, Náfrádi B, Bernard L, Bonvin E, Gaál R, Magrez A, Forró L and Horváth E 2015 Microengineered $\text{CH}_3\text{NH}_3\text{PbI}_3$ nanowire/graphene phototransistor for low-intensity light detection at room temperature *Small* **37** 4824–8